I&EC research
Industrial & Engineering Chemistry Research

pubs.acs.org/IECR
Article

Eliminating the Need for Branching and Chain Extender Additives in PET Foaming Process by Exploiting CO_2-Induced Crystals with 3D-Foam Printing

Lorenzo Lombardi,* Claudio Esposito, Daniele Tammaro, Odda Ruiz de Ballesteros, and Pier Luca Maffettone

Cite This: *Ind. Eng. Chem. Res.* 2025, 64, 12770−12780
Read Online

ABSTRACT: Polyethylene terephthalate (PET) is a versatile and widely utilized thermoplastic with a significant presence in various industries, including textiles, packaging, construction, membrane filtration, and biomedical applications. This study demonstrates the feasibility of an innovative additive-free 3D foam printing technology for PET, utilizing preinduced crystals from CO_2 impregnation to produce high-quality foam structures. By optimizing extrusion speed and hot-end geometry, the process effectively controls foam morphology, eliminating the need for branching agents or chain extenders. The mechanical properties of the foamed strands were systematically analyzed, revealing that the mechanical properties are strongly influenced by the degree of foaming, crystallinity, and relative density. To account for this effect, a modified scaling law was introduced, incorporating the influence of crystals on stiffness. The model accurately describes the elastic modulus across a wide range of densities and provides a useful tool for predicting mechanical properties. The methodology is readily applicable to commercially available PET and standard 3D printing technology, making it a scalable and practical solution for lightweight structured materials in diverse industries. The findings highlight the critical role of process-induced crystallinity in enhancing the mechanical properties of foamed PET, offering a scalable, cost-effective, and sustainable method for lightweight polymer manufacturing. This approach eliminates the reliance on chemical additives while optimizing foam performance, making it highly relevant for industrial applications requiring high-performance lightweight materials.

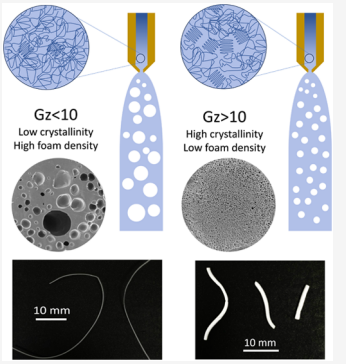

1. INTRODUCTION

Polyethylene terephthalate (PET) is a widely used thermoplastic polymer with applications spanning textiles,[1] packaging,[2] construction,[3] membrane filtration,[4] and biomedical devices.[5] Due to its broad utility, PET contributes significantly to global plastic consumption, representing approximately 8% by weight and 12% by volume of total solid waste.[1] Its excellent temperature resistance, high impact strength, and dimensional stability make semicrystalline PET a cost-effective and reliable engineering thermoplastic.[6]

Beyond conventional uses, PET is also processed into foams for structural applications such as wind turbine blades[7] and train compartment panels.[8] Extrusion foaming is the primary manufacturing route for PET foams,[9,10] as well as for other thermoplastics.[11] However, PET foaming remains technically challenging due to its inherently low melt strength and slow crystallization rate,[12] which can lead to foam collapse and poor structural uniformity.

Crystallinity plays a key role in addressing these limitations. It facilitates bubble nucleation by offering heterogeneous sites[13−15] and helps retain the blowing agent, thereby improving foam uniformity. A particularly effective method to enhance crystallinity is carbon dioxide (CO_2) impregnation, which can induce crystal formation even at room temperature.[16,17] These CO_2-induced crystals lower the Gibbs free energy barrier for bubble formation,[18,19] and if retained during processing, they can contribute to increased melt strength.

To further improve PET foamability, several studies have explored the use of chain extenders and branching agents.[20−22] For instance, the addition of 0.75% pyromellitic dianhydride (PMDA) has been shown to significantly enhance zero-shear viscosity and melt strength.[23] Likewise, introducing long-chain branching (LCB) structures has been found to increase cell density and reduce cell size, leading to improved foam morphology.[12] Modified PET copolymers have also enabled the production of low-density foams with superior properties.[24,25]

In addition to chemical modifications, foam morphology can be refined by adding nucleating agents such as talc or carbon black.[26,27] Xi et al.[26] demonstrated that PET/clay nano-

Received: March 17, 2025
Revised: June 3, 2025
Accepted: June 5, 2025
Published: June 11, 2025

composites, despite lower viscosity compared to PMDA-modified PET, achieved good foam stability due to well-dispersed clays. Bocz et al.[27] found that talc increased the crystallization temperature and yielded smaller, more uniform cells, resulting in foams with higher porosity and enhanced stability.

Despite these developments, a persistent challenge remains: CO_2-induced crystals often dissolve during extrusion, eliminating their beneficial effects precisely when they are most needed for foaming. As a result, existing strategies have largely focused on generating new crystals near the die or incorporating additives to restore melt strength and nucleation capability. However, these approaches frequently overlook the potential of preserving and utilizing the crystals already present in the polymer matrix.

Building on this gap, the central hypothesis of this study is that CO_2-induced crystals can be preserved and effectively leveraged during the foaming process, without the need for additives or branching agents. We demonstrate that by precisely controlling the polymer thermal profile within a commercial 3D printer—specifically through adjustments to printing speed and nozzle geometry—it is possible to regulate the extent of crystal melting in the hot-end. This approach enables direct manipulation of foam morphology using unmodified, linear PET. The observed improvements in foam structure are attributed to the presence of residual CO_2-induced crystals, which serve as heterogeneous nucleation sites during bubble formation.

2. MATERIALS AND METHODS

2.1. Filament Preparation. In this study, we present additive-free PET foamed strands produced using an innovative 3D foam printing technology. Multiple experiments were conducted, varying both the extrusion speed and the diameter of the 3D printer hot-end. We utilized NEOPET 82 from Neogroup, and an overview of its physical properties can be found in Table 1. Prior to any handling, the PET pellets were dried for 6 h at 70 °C.

Table 1. Physical Properties of NEOPET 82

property	value	test method
intrinsic viscosity (IV)	0.82 ± 0.02 dl/g	WN-B010-7040 D (capillary visc.)
melting temperature (Tm)	248 ± 4 °C	WN-B010-7089 D (DSC)
acetaldehyde content (AA)	≤ 1 ppm	WN-B010-9013 D (GC)
color b	≤ 1	WN-B010-7136 D (HUNTER Lab)
fines	≤ 50 ppm	WN-B010-9031 D
water content	≤ 0.2%	WN-B010-7159 D
pellets weight	1.7 ± 0.1 g/ 100 pellets	WN-B010-9038 D

To achieve a unified single-stage foaming process during printing, the following sequential steps are executed: (1) extruding filaments from PET pellets, (2) incorporating the blowing agent into the filament, (3) generating a foamed strand using the 3D printer, and (4) stabilizing the resulting foamed filament.

To produce a PET filament with a diameter of d_f = 1.5 mm, we employed a Composer350 extruder from the 3DEVO company (The Netherlands), and the process parameters are detailed in Table 2. The extruded PET filament was exposed to a 6 MPa

Table 2. Filament Extrusion Process Conditions

screw speed	Zone 1 (feeding) temperature	Zone 2 (melting) temperature	Zone 3 (mixing) temperature	Zone 4 (shaping) temperature	fan speed
10 rpm	280 °C	285 °C	287 °C	290 °C	500 rpm

CO_2 environment for 8 days to achieve complete CO_2 solubilization, based on a CO_2 diffusion coefficient of $D = 7 \cdot 10^{-13}$ m^2/s at 25 °C,[13] and to produce uniformly crystalline samples.[13]

2.2. Filament Foaming. A Prusa Research I3 Mk3s 3D printer was employed for foaming the filament. The diameter of the hot-end of the 3D printer was adjusted to regulate the temperature profile within the melt. The samples were processed using the 3D printer immediately after extraction from the CO_2 pressurized chamber to prevent CO_2 desorption. This step was crucial to avoid the formation of concentration gradients along the radial direction, which could have led to the development of gradient foams.[28,29] The foaming process was conducted with the hot-end temperature maintained at 290 °C for all samples.

The foams underwent characterization to determine their bulk density (ρ_b) and cell density (N). The bulk density was measured in accordance with ASTMD7710, employing an analytical balance (Mettler Toledo, Columbus, OH). To prepare the samples, they were initially sectioned with a razor blade and subsequently coated with gold via a sputter coater. The cellular structure of the foams was examined using a scanning electron microscope (Hitachi TM 3000 SEM). The SEM images presented in the manuscript were captured from randomly chosen cross sections of the foamed samples. Each SEM experiment was conducted at least three times using three different samples to calculate the cell size distribution. N was computed as:

$$N = \frac{\rho}{\rho_b}\left(\frac{n}{A}\right)^{3/2} \tag{1}$$

where ρ represents the density of the solid sample, and n corresponds to the number of cells within the selected area A on the SEM micrograph. The expansion ratio was computed as ρ/ρ_b, and the diameter ratio as d_f/d_n, where d_f is the foamed strand diameter and d_n is the nozzle diameter (d_n = 0.6 mm).

To assess the cell size distribution within the cross-sections of the samples, a custom MATLAB algorithm was employed. First, the foam cross-section images acquired via SEM were binarized. The algorithm then automatically detects and outlines the individual foam cells based on the identified boundaries in the binarized image. Next, using the total number of detected cells and the cross-sectional area, the program calculates the cell density by applying eq 1. Finally, the algorithm generates the cell size distribution by measuring and cataloging the characteristic dimensions (e.g., equivalent diameter D_{eq}) of each detected cell. This process enables a detailed characterization of the foam morphology.

2.3. Thermal Analysis. Differential Scanning Calorimetry (DSC) was performed to evaluate the thermal behavior of the polymer samples. The measurements were conducted using a DSC 3+ Mettler Toledo, equipped with an IntraCooler III refrigeration system, under a nitrogen atmosphere to prevent thermal degradation. Samples were subjected to a controlled heating ramp from 25 to 300 °C at a rate of 10 °C/min. This

https://doi.org/10.1021/acs.iecr.5c01123
Ind. Eng. Chem. Res. 2025, 64, 12770−12780

heating protocol was designed to capture key thermal transitions, including the glass transition temperature (T_g), crystallization temperature (T_c), and melting temperature (T_m). The degree of crystallinity (χ_c) of the materials was determined from the first heating scan as

$$\chi_c = \frac{\Delta H_m - \Delta H_{cc}}{\Delta H_c^0} \quad (2)$$

where ΔH_m, and ΔH_c^0 are the experimental and the thermodynamic equilibrium melting enthalpies of PET crystals, respectively, and ΔH_{cc} is the enthalpy associated with the cold crystallization peak. The value of ΔH_c^0 = 140 J/g has been assumed.[30]

2.4. Mechanical Properties. The mechanical properties of the foamed strands were evaluated through compression tests conducted using a commercial texture analyzer (Brookfield Ametek CTX). The strands were cut into thin cylindrical samples with a height of approximately 0.5—1 mm. The samples were then fixed onto a plate and subjected to compressive stress, reaching up to 50% deformation, with the upper plate moving at a constant velocity of 0.01 mm/s.

2.5. Hot-End Geometry. This study examined two distinct hot-end designs, both featuring an internal channel but differing primarily in channel diameter distribution. The hot-end, positioned just before the nozzle exit (Figure 1a), is heated by a resistance element. Within this component, the polymer flows through a cylindrical channel, where it undergoes the melting process.

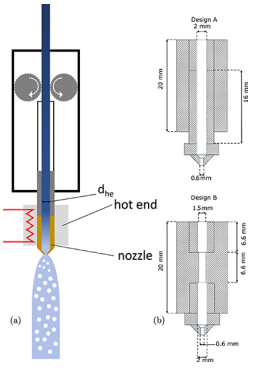

Figure 1. (a) Sketch of the PET filament entering the hot-end and foaming upon the 3D printer nozzle exit. (b) Schematic representation of the two hot-end designs. (Top) Design A, (Bottom) Design B. The sketch is not to scale.

The experiments were designed to regulate the extent of PET crystal melting within the hot-end, directly influencing foaming behavior. The first design (A) features a Volcano-style nozzle, incorporating a 2 mm inner channel that remains cylindrical throughout the 20 mm length of the hot-end. The channel then converges to 0.6 mm at the nozzle exit. This nozzle is in direct contact with the heat break, ensuring a consistent 2 mm diameter throughout the hot-end length before tapering at the exit. The second design (B) incorporates a variable-diameter channel over the same 20 mm length. The first third consists of the heat break, which has a 2 mm inner diameter. The middle third narrows to 1.5 mm, resembling the design described in.[31] The final third is composed of a shorter nozzle with a 2 mm inner channel, which then tapers down to 0.6 mm at the exit. This configuration maintains a 2 mm diameter at the entrance and exit while introducing a restricted flow region in the middle.

Upon exiting the nozzle, the polymer melt undergoes an abrupt pressure reduction, serving as the primary trigger for foaming. The resulting foamed strand is then cooled using a fan and gathered for analysis. All foams have undergone characterization based on expansion ratio, diameter ratio, cell density, and degree of crystallinity.

2.6. Rheology. Rheological characterization was carried out using an **Anton Paar MCR 702** rheometer with a 25 mm parallel plate geometry at 290 °C. The sample was allowed to equilibrate at the test temperature for 10 min to ensure complete melting. Two tests were performed: a nonlinear flow curve to evaluate the shear-dependent viscosity, and a linear viscoelastic frequency sweep to assess the molecular structure and linearity of the PET chains. Prior to the frequency sweep, an amplitude sweep was conducted to verify the linear viscoelastic (LVE) region, confirming that a strain amplitude of 1% falls within it. The flow curve results are reported in the main manuscript, while the frequency sweep data—obtained at a constant strain amplitude of 1%—are presented in the Supporting Information.

3. RESULTS

It is well established that the diffusion of CO_2 into PET promotes crystal growth.[13,17] Studies have shown that achieving a steady-state crystallinity in PET at 25 °C and 6 MPa requires approximately one day, following the establishment of a uniform CO_2 concentration throughout the sample.[13]

It is also important to note that the PET used in this study consists of linear chains without branching, as confirmed by the rheological analysis presented in the Supporting Information and discussed in detail in ref.32

The DSC heating scans for PET both before and after CO_2 solubilization are shown in Figure 2. After the inflection point due to T_g at 70 °C the DSC scan of the PET sample without blowing agent exhibits a cold crystallization peak at 117 °C, followed by a melting peak at 250 °C. In the presence of CO_2, only the inflection point of T_g at 63 °C and the melting peak at 250 °C are observed, indicating that the sample is crystalline.

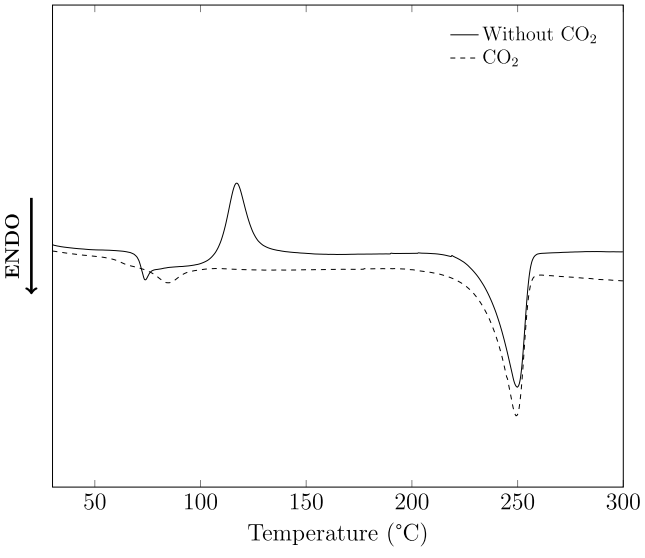

Figure 2. DSC heating scans of PET filament before and after CO_2 solubilization at 60 bar. The degree of crystallinity χ_c is 0.11 and 0.28 for PET without and with CO_2, respectively.

https://doi.org/10.1021/acs.iecr.5c01123
Ind. Eng. Chem. Res. 2025, 64, 12770−12780

Notably, the glass transition temperature (T_g) decreases from 70 to 63 °C in the presence of CO_2, likely due to its plasticizing effect. The degree of crystallinity χ_c is 0.11 and 0.28 for PET without and with CO_2, respectively. This confirms that PET has a relatively high crystal content as a result of CO_2 solubilization.

The following sections discuss the effect of process parameters, including extrusion speed and hot-end diameters, on foam quality. Additionally, they explore the correlation between these parameters and the crystal content within the foam.

3.1. Effect of Extrusion Speed. Figure 4 illustrates the impact of extrusion speed (U) on expansion ratio, diameter ratio, cell density, and degree of crystallinity is presented. An increase in U leads to an increased expansion ratio (Figure 4a) and diameter ratio (Figure 4b) for each hot-end diameter. This trend is consistent with previous findings in PET extrusion foaming,[33] where it was attributed to a higher pressure drop rate (PDR) during printing. In this context, the PDR is the rate at which the pressure in the nozzle decreases to ambient pressure as the polymer exits.

An increase in U also leads to a higher pressure drop in the nozzle while simultaneously reducing the residence time, resulting in an increased PDR. In this study, U is varied between 0.5 and 45 mm/s. A rough estimate of the pressure drop rate is given by PDR $\approx 8\eta\, Q^2/\pi^2(d_n/2)^6$, where $Q = U\pi\, d_f^2/4$ represents the polymer flow rate, and η is the viscosity of PET. The nonlinear rheology measurements are shown in Figure 3. Using these values, the PDR is estimated to vary within the range $O(10^2)-O(10^3)$ bar/s.

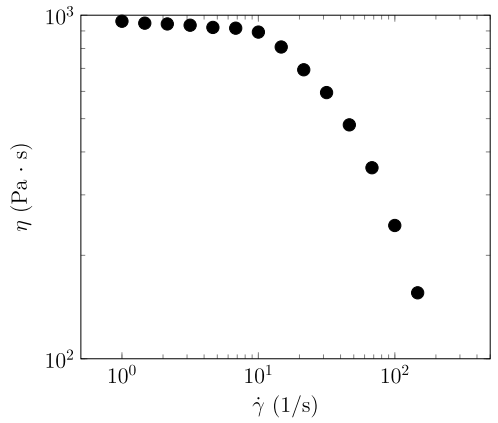

Figure 3. Viscosity as a function of shear rate for NEOPET 82 at 290 °C.

SEM analysis shown in Figure 5, reveals that higher printing velocity increases the number of cells per unit volume (Figure 4c) while decreasing the average bubble size (Figure 10) across all hot-end diameters. Within the velocity range investigated in this study, cell density varies by more than 3 orders of magnitude. This finding aligns with the behavior observed in PET foam extrusion processes.[33] Typically, this behavior is associated with an increase in PDR.[34] A higher PDR accelerates the formation of stable nuclei, reducing the likelihood of the blowing agent inflating newly formed bubbles and leading to a more refined cellular structure.[34]

A similar trend is observed for the degree of crystallinity obtained from DSC analysis Figure 6. Regardless of the hot-end diameter, χ_c increases monotonically with U, as shown in Figure 4d. This is likely due to the fact that when the extrusion rate increases, the residence time of the PET in the "hot-end" decreases, preventing already-formed crystals from melting and allowing more crystals to survive until the nozzle exit.

Compression tests highlight a significant influence of U on the maximum stress (σ_{max}) reached at the end of the linear elastic regime. As illustrated in Figure 7, σ_{max} decreases by nearly an order of magnitude with increasing U for both hot-end geometries. This trend aligns with findings from previous studies, which report a deterioration in the mechanical properties of foamed PET under compression as the expansion ratio increases, corresponding to a decrease in foam density.[35,36] Similar behavior has also been observed in tensile strength measurements of foamed PLA strands.[28,37]

However, the specific mechanical properties (σ_{max}/ρ_b) of the foamed strands exhibit a significantly smaller decrease with increasing printing velocity compared to σ_{max}. This improvement can be attributed to the enhanced crystallinity of the foamed samples at higher printing velocities, as shown in Figure 4d. A more detailed analysis of this phenomenon will be provided in Section 4.

3.2. Effect of Hot-End Diameter. As mentioned earlier, in this study we varied the hot-end diameter (d_{he}) between two values: 1.5 mm and 2 mm. Figure 4 presents the impact of d_{he} on expansion ratio, diameter ratio, cell density, and degree of crystallinity. Generally, the expansion ratio is greater for the larger diameter (Figure 4a), and the same behavior is observed for the cell density (Figure 4c). The diameter ratio appears to be less sensible to the hot-end diameter; however, an increase in this parameter is observed for U values greater than 25 mm/s (Figure 4b).

The observed increase in χ_c (Figure 6) with larger hot-end diameters is primarily attributed to diminished heat transfer efficiency to the polymer melt core. As the hot-end diameter (d_{he}) increases, the radial distance between the heated barrel wall and the center of the polymer stream also increases. Under constant residence time and thermal diffusivity, this extended distance impedes effective thermal conduction, thereby delaying heat penetration into the core. As a result, the melting of CO_2-induced crystalline domains becomes incomplete, leading to a higher retention of crystallites and, consequently, an elevated degree of crystallinity at the nozzle exit. This mechanism and its implications will be further examined in Section 4.

Concerning the mechanical properties of the foamed strands at low printing velocities, the hot-end diameter (d_{he}) does not appear to have a significant influence, as both σ_{max} and σ_{max}/ρ_b exhibit similar values for the two hot-end geometries (Figure 7). However, at higher printing velocities (U), a noticeable trend emerges where the mechanical properties slightly improve for samples printed with the smaller hot-end diameter (d_{he} = 1.5 mm). This will be discussed in Section 4.

4. RESULTS, DISCUSSION, AND MODELING

Results similar to those reported here have been linked to an increase in PDR with U, which subsequently promotes bubble nucleation. A 10-fold increase in PDR (Section 3.1) results in a cell density increase of approximately 10^3, as illustrated in Figure 4c. However, it has been shown that an increase in PDR alone cannot account for the significant rise in cell density observed in this study.[34] This suggests the possibility of additional mechanisms contributing to the sharp increase in bubble nuclei observed in the experiments.

Another widely used approach to enhance bubble nucleation in polymers is the incorporation of additives, or nucleating

https://doi.org/10.1021/acs.iecr.5c01123
Ind. Eng. Chem. Res. 2025, 64, 12770−12780

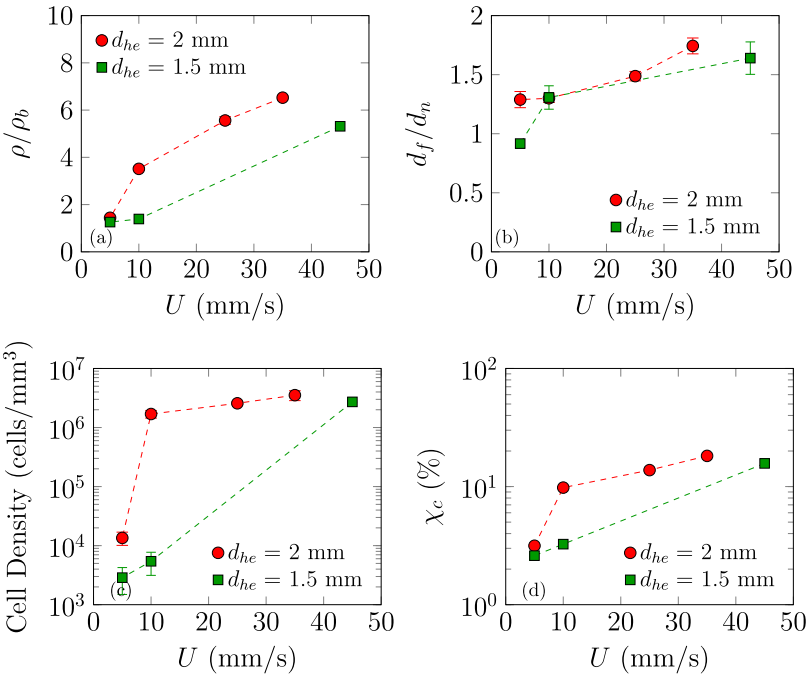

Figure 4. (a) Expansion ratio of foamed samples as a function of extrusion velocity for two different hot-end diameters. (b) Diameter ratio as a function of extrusion velocity for two different hot-end diameters. (c) Number of cells per unit volume in the foamed samples as a function of extrusion velocity for two different hot-end diameters. (d) Degree of crystallinity of foamed samples as a function of extrusion velocity for two different hot-end diameters.

agents. These agents facilitate heterogeneous bubble nucleation by creating stable nuclei on their surfaces. For instance, talc particles have been demonstrated to increase the cell density of polystyrene by roughly 3 orders of magnitude,[34] a magnitude comparable to the increase observed in this study. The rise in the degree of crystallinity with U and d_{he} may mimic the behavior of commercial nucleating agents, thereby enhancing bubble heterogeneous nucleation. This is further facilitated by the significantly lower contact angle between the crystals and the liquid phase compared to standard nucleating agents like talc.[19]

The quantity of crystals in foam produced through 3D printing is closely tied to the temperature profile within the polymer in the hot-end, which is governed by the process parameters adjusted in this study. Although variations in PDR can affect foam density and morphology, its impact is relatively minor compared to that of crystallinity, particularly at the highest extrusion speeds. In the 3D printer, the polymer filament melts within the hot-end as heat is applied. At higher extrusion speeds, the polymer residence time in the hot-end decreases, resulting in a nonuniform temperature distribution in the radial direction. As a result, the core of the filament does not reach the same temperature of the polymer-wall interface, which is equal to the imposed temperature. This uneven heating prevents the complete melting of all of the crystals initially present in the filament during the printing process.

This highlights the need to identify a parameter that represents the temperature nonuniformity within the filament, as the PDR alone cannot account for the observed trends. The uniformity of temperature in the hot-end is determined by the ratio between convective axial heat flux and conductive radial heat flux, known as the Graetz number (Gz),[38] defined as

$$\mathrm{Gz} = \frac{\rho c_p U \overline{R_{he}}^2}{k_{eq} L} \tag{3}$$

where c_p is the specific heat, k_{eq} is the equivalent thermal conductivity, $\overline{R_{he}}$ is the hot-end average radius, and L is the hot-end length.

As mentioned earlier, two different hot-end geometries have been used in this study. For hot-end A, the filament diameter of 1.5 mm is insufficient to completely fill the hot-end (2 mm), likely creating a thin air gap between the filament and the heated wall of the hot-end. This must be considered when computing k for the Graetz number. Given k = 0.19 W/m°C for PET and using the equivalent thermal conductivity k_{eq} resulting from two thermal resistances in series (one for PET and one for air), we obtain k_{eq} = 0.07 W/m°C. This thermal conductivity is treated as constant for the entire length of the hot-end. In contrast, for hot-end B, only the initial third of its length would not be completely filled, resulting in an overall k_{eq} = 0.15 W/m°C.

In 3D printing, if $Gz < 10$, the conductive heat flux is sufficient to heat the polymer core to the wall temperature by the end of the hot-end.[38] However, if $Gz > 10$, the temperature profile in the polymer is not homogeneous, as convective heat transfer dominates over conductive heat transfer. The Graetz number is particularly useful for visualizing the effects of both U and $\overline{R_{he}}$ on foaming performance. The dependence of the temperature profile on Gz is also confirmed by numerical simulations presented in the Supporting Information.

As illustrated in Figure 9, the proposed nondimensionalization effectively collapses the data onto a single curve. As shown in Figure 9d, at $Gz < 10$, the crystal content in the foamed samples remains relatively low, indicating predominantly amorphous PET. In contrast, at $Gz > 10$, the crystal content increases significantly. This rise in crystallinity is attributed to the emergence of substantial thermal gradients within the hot-end, which lead to temperature nonuniformity, as confirmed by previous studies.[38] This thermal nonuniformity prevents the complete melting of PET crystals, thereby promoting

https://doi.org/10.1021/acs.iecr.5c01123
Ind. Eng. Chem. Res. 2025, 64, 12770−12780

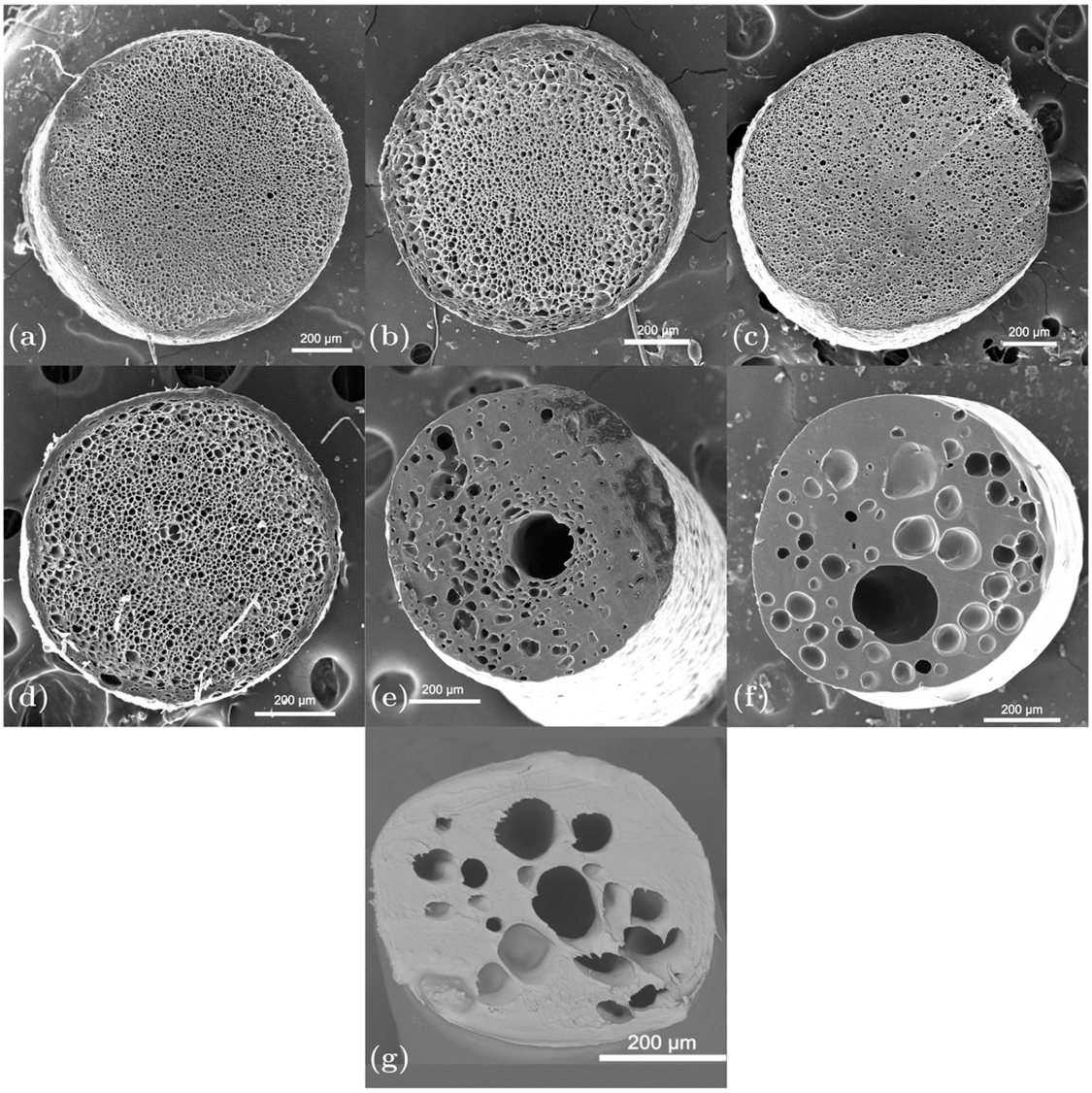

Figure 5. SEM micrographs of the radial section of foamed PET samples produced at various process conditions. Parameters include plunger velocity (U), hot-end diameter (d_{he}), and Graetz number (Gz): (a) U = 35 mm/s, d_{he} = 2 mm, Gz = 38; (b) U = 25 mm/s, d_{he} = 2 mm, Gz = 27; (c) U = 45 mm/s, d_{he} = 1.5 mm, Gz = 20; (d) U = 10 mm/s, d_{he} = 2 mm, Gz = 11; (e) U = 5 mm/s, d_{he} = 2 mm, Gz = 5; (f) U = 10 mm/s, d_{he} = 1.5 mm, Gz = 4; (g) U = 5 mm/s, d_{he} = 1.5 mm, Gz = 2.

heterogeneous bubble nucleation and enhancing melt strength. As a result, uniformly foamed structures are obtained, as evidenced by the SEM micrographs in Figure 5. This behavior is also consistent with fundamental findings from nonaqueous foaming studies, which show that foam stability increases with viscosity.[39] Conversely, for Gz < 10, the temperature within the hot-end remains uniform across the radial direction and equal to the wall temperature, leading to the complete melting of crystals and to an almost unfoamed structure. The proposed mechanism is schematized in Figure 8a.

Figure 9a illustrates the relationship between the expansion ratio and Gz. As anticipated, the expansion ratio increases with Gz. At Gz < 10 foam expansion is quite poor with expansion ratio values close to unity (Figure 8b), as confirmed by the SEM images of samples extruded at low Gz number Figure 5. At Gz > 10, there is a sudden rise in the expansion ratio, indicating the presence of temperature inhomogeneity at these Gz values (Figure 8c).

A comparable trend is observed in Figure 9c, which illustrates cell density as a function of Gz. For Gz < 10, the cell density remains relatively low, approximately 10^3 cells/mm^3. However, when Gz > 10, the cell density increases dramatically by 3 orders of magnitude, indicating that residual crystals play a crucial role in enhancing bubble nucleation.

In contrast, the diameter ratio shows a steady increase with Gz but does not exhibit a pronounced rise for Gz > 10, as depicted in Figure 9b. This behavior can likely be attributed to anisotropic expansion during significant foaming. In this case, the polymer tends to expand more in the axial direction than in the radial direction, thereby preventing a sharp increase in the diameter ratio.

The cell size distribution is also dependent on Gz, as shown in Figure 10, which presents the probability distribution of cell size (D_{eq}) for different values of Gz.

For Gz < 10, the cell size distribution is relatively broad, with sizes ranging from 5 to 100 μm. As Gz increases (Gz > 10), the distribution becomes progressively narrower, with most cell

https://doi.org/10.1021/acs.iecr.5c01123
Ind. Eng. Chem. Res. 2025, 64, 12770−12780

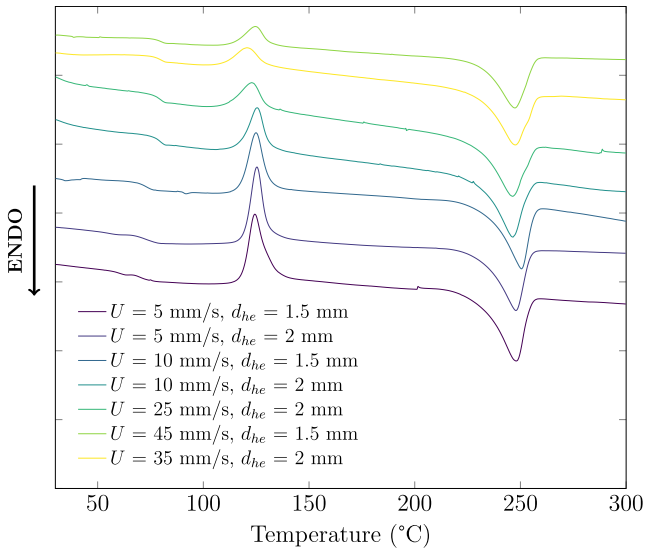

Figure 6. Differential scanning calorimetry (DSC) curves of PET samples printed at various extrusion speeds (U) and hot-end diameters (d_{he}). Each curve is vertically offset for clarity. The direction of increasing endothermic heat flow is indicated by the arrow. Key thermal transitions, including crystallization and melting peaks, vary as a function of processing conditions.

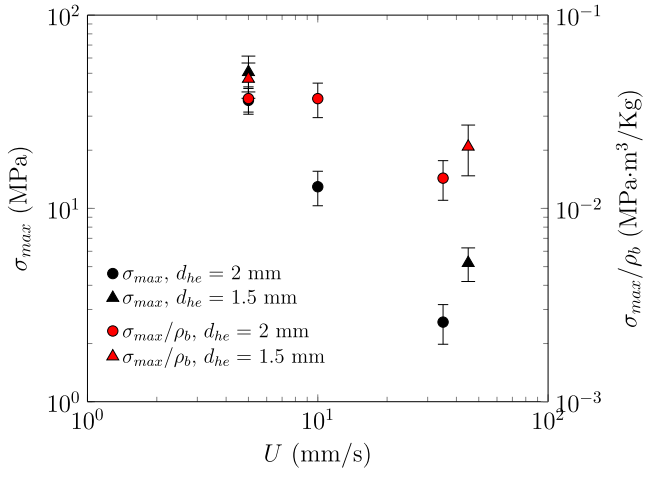

Figure 7. Maximum stress (σ_{max}) and specific maximum stress (σ_{max}/ρ_b) as functions of printing velocity for foamed PET strands printed with two different hot-end diameters.

sizes concentrated below 20 μm (D_{eq} < 20 μm). At higher Gz values, the variability in cell sizes decreases, with fewer large cells and a sharper peak at smaller D_{eq}, indicating a more uniform bubble size distribution. This shift toward smaller, more uniform cell sizes suggests that higher Gz enhances consistent bubble nucleation while limiting cell growth. This behavior is likely due to increased thermal gradients, which promote higher crystallinity and greater melt strength in the polymer. These findings highlight the significant role of Gz in regulating bubble nucleation and growth, leading to finer, more uniform foamed structures at elevated Gz values.

A similar analysis can be applied to interpret the results of foam compression tests. The complete stress (σ)-strain (ϵ) curves are presented in Figure 11a, illustrating the distinct mechanical behavior between nonfoamed and foamed samples. The unfoamed material exhibits the highest mechanical performance, characterized by a steep linear increase in stress, followed by strain hardening beyond approximately 20% strain—a typical response of dense polymers with high load-bearing capacity. As Gz increases, corresponding to a greater degree of foaming, the mechanical properties degrade significantly. The stress levels drop substantially, and the material reaches stress saturation at lower strains, indicating reduced stiffness and strength. The progressive decline in peak stress with increasing Gz further confirms that higher foaming degrees (lower densities) lead to weaker mechanical performance. This trend aligns with previous studies linking an increased expansion ratio to reduced mechanical strength due to a higher fraction of voids in the material.[35,36] In contrast to nonfoamed or minimally foamed samples (Gz < 10), where stress continues to increase beyond 20% strain, highly foamed samples exhibit a plateau, suggesting that their deformation is predominantly governed by cell collapse rather than strain hardening.

Plotting σ_{max} and σ_{max}/ρ_b against Gz allows the data to collapse onto a single curve, demonstrating that the chosen nondimensionalization effectively captures the underlying physics of the phenomenon under investigation. The maximum stress recorded at the end of the linear elastic regime during compression decreases consistently with increasing Gz, confirming that higher degrees of foaming weaken the mechanical properties due to the presence of air voids. However, as previously observed, the reduction in specific mechanical properties with Gz is significantly less pronounced. This suggests that while foaming reduces absolute strength, the corresponding decrease in density helps maintain a relatively stable strength-to-weight ratio. Thus, although foaming weakens the material in absolute terms, the reduction in density mitigates the performance loss when considering mechanical efficiency relative to weight. This trend is particularly relevant for applications where lightweight structures are prioritized over absolute strength. The data also suggests that at low Gz, the reduction in mechanical properties is minimal, whereas at higher Gz, the decrease in σ_{max} becomes more significant. This observation implies a possible threshold around Gz ≈10, beyond which excessive foaming leads to structural weaknesses.

The observed trend in σ_{max}/ρ_b can be attributed to the high crystallinity content at elevated Gz values. This hypothesis is further supported by an analysis of the elastic modulus. Figure 11c presents the specific elastic modulus (ϵ/ϵ_p), where ϵ and ϵ_p represent the elastic moduli of the foamed and pure polymer, respectively, plotted as a function of the inverse expansion ratio (ρ_b/ρ). The data follows a power-law trend up to ρ_b/ρ ≈0.4, as indicated by the solid line, demonstrating that a decrease in ρ_b/ρ leads to a corresponding decrease in the specific elastic modulus. This behavior is consistent with classical scaling laws for cellular materials, where the specific elastic modulus follows the relationship $\epsilon/\epsilon_p \sim (\rho_b/\rho)^2$,[40] which perfectly describes our data.

At lower ρ_b/ρ, however, the data begins to deviate from the expected power-law trend and stabilizes at a higher value. This deviation suggests the presence of an additional stiffening mechanism that prevents the elastic modulus from decreasing as rapidly as predicted by a simple porosity-based scaling law. The enhanced elastic modulus of the foamed PET strands at low densities can be attributed to increased crystallinity at higher degrees of foaming. This explanation is further supported by the observed trend in specific crystallinity (χ_c/χ_c^p), where χ_c represents the degree of crystallinity of the foamed strand and χ_c^p that of unfoamed PET after CO_2 solubilization. As shown in Figure 11d, χ_c/χ_c^p decreases as a function of the inverse

https://doi.org/10.1021/acs.iecr.5c01123
Ind. Eng. Chem. Res. 2025, 64, 12770−12780

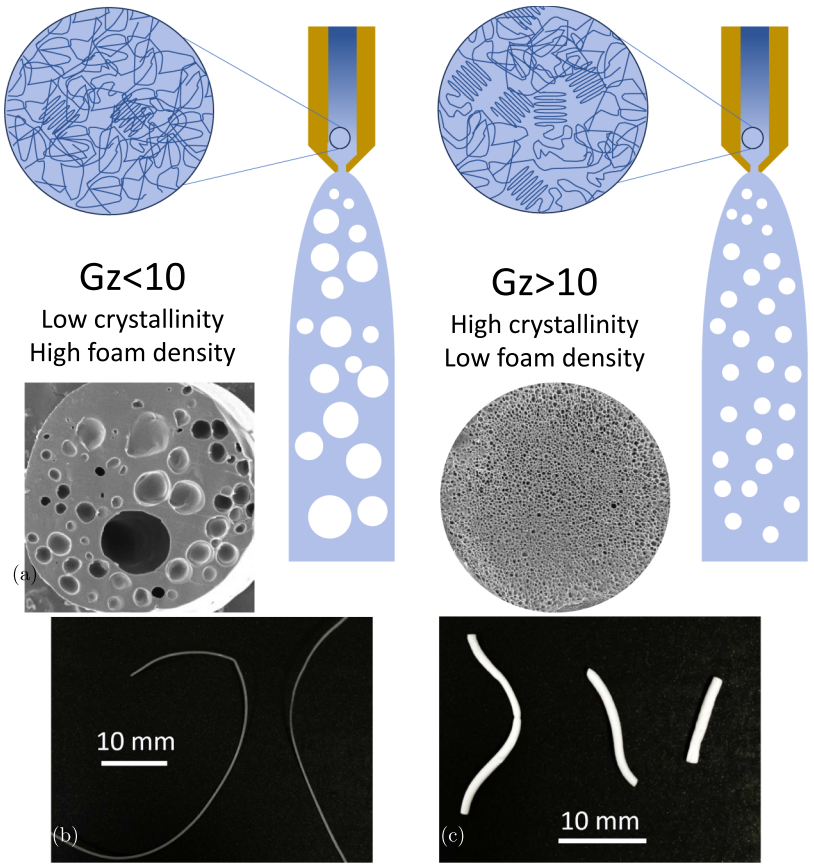

Figure 8. (a) Schematic depicting the crystalline structure and its impact on foam quality at varying *Gz* number. (b) Picture of foamed filament at *Gz* = 5. (c) Picture of foamed filament at *Gz* = 38.

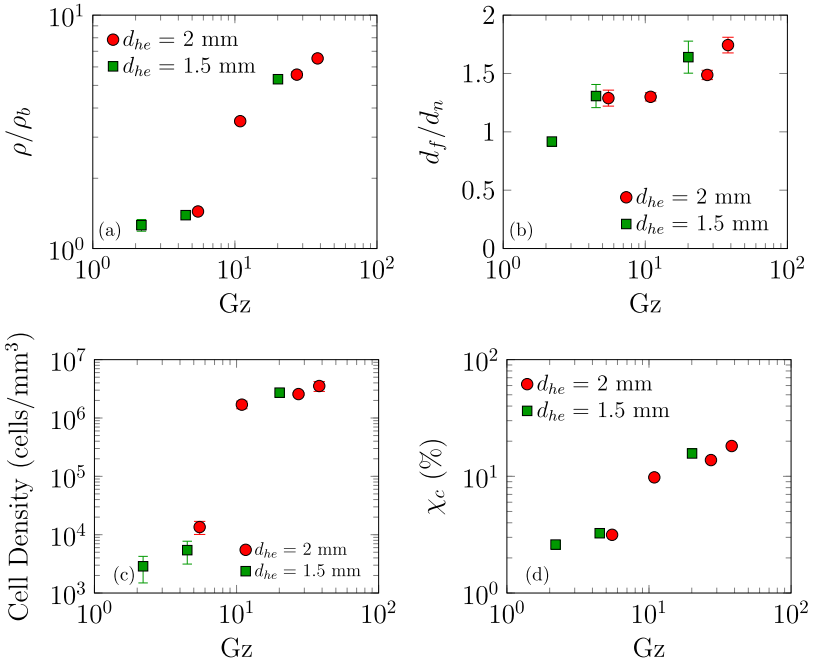

Figure 9. (a, b, c, d) Expansion ratio, diameter ratio, cell density per unit volume, and degree of crystallinity of foamed samples as a function of *Gz* for two different hot-end diameters, respectively.

expansion ratio (ρ_b/ρ). The data follows a power-law decay, $\chi_c/\chi_c^p \sim (\rho_b/\rho)^m$, with an exponent $m = -1.14$ obtained through best fitting, which contrasts with previous findings reporting a linear decrease.[37]

At higher relative densities, the material retains a greater number of crystalline regions, which contribute to its overall stiffness.[41] These crystalline domains likely reinforce the cell walls, enhancing the material load-bearing capacity and leading

https://doi.org/10.1021/acs.iecr.5c01123
Ind. Eng. Chem. Res. 2025, 64, 12770−12780

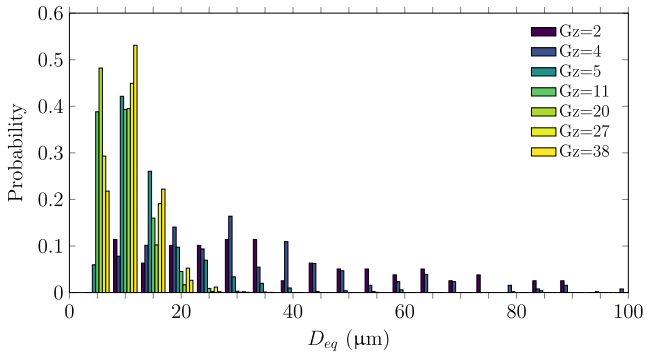

Figure 10. Cell size distribution probability of foamed samples at different *Gz*.

to the observed stabilization of the elastic modulus at low ρ_b/ρ. To account for this effect, the classical scaling law proposed by[40] can be modified. By incorporating the exponents obtained from the scaling of χ_c/χ_c^p ($m = -1.14$), we introduce an additional contribution to ρ_b/ρ and include a power-law prefactor K, resulting in the following modified scaling equation

$$\frac{\epsilon}{\epsilon_p} = \left(\frac{\rho_b}{\rho}\right)^2 + K\left(\frac{\rho_b}{\rho}\right)^m \tag{4}$$

As shown in Figure 11c, this modified scaling, with $K = 0.0033$, provides a satisfactory fit to the data. It thus enables the prediction and design of the mechanical properties of foamed printed strands over a wide range of densities, while also accounting for the significant influence of crystallinity on the elastic modulus. Similar scaling approaches have been successfully applied to describe the mechanical properties of microfoamed polymer strands, under the assumption that cell orientation remains consistent across samples of different densities, as illustrated in Figure 5.[37] However, caution should be exercised when applying eq 4 to extrapolate mechanical behavior at even lower ρ_b/ρ. When the polymer content becomes negligible compared to the gas content, the physical assumptions underlying this scaling may no longer hold, potentially limiting its validity in highly expanded foams.

It is important to note that although this study focuses on isolating the effect of heat transport in the hot-end via the Graetz number (*Gz*), other parameters—such as CO_2 concentration, saturation pressure, time, and hot-end temperature—are also well-known to significantly influence the foaming behavior of PET and related polymers. Prior work has shown that increasing CO_2 content enhances crystallinity through a plasticizing effect,[13] which in turn improves foam morphology and cell uniformity in both PET[36] and PLA.[37] Additionally, optimal foaming temperatures have been identified for PET,[33] PLA,[37,38] and olefin block copolymers,[11] with suboptimal conditions either suppressing nucleation or causing excessive cell coalescence and collapse. In this study, these factors were kept constant to isolate the role of thermal transport as characterized by *Gz*. Future work will examine their combined effects to map optimal foaming conditions and further validate the link between crystallinity and mechanical performance.

5. CONCLUSIONS

This work introduces a novel additive-free 3D foam printing strategy for polyethylene terephthalate (PET), utilizing CO_2-induced crystallinity to enable high-quality foam structures without the need for branching agents or chain extenders. By systematically tuning the extrusion speed and hot-end geometry, the process allows effective control over foam morphology and mechanical properties, using only commercially available PET and standard 3D printing equipment.

A key contribution of the study is the demonstration that residual crystallinity—induced by CO_2 saturation and partially retained during printing—plays a critical role in bubble nucleation and foam stabilization. The thermal profile within the printer hot-end, quantified via the Graetz number (*Gz*),

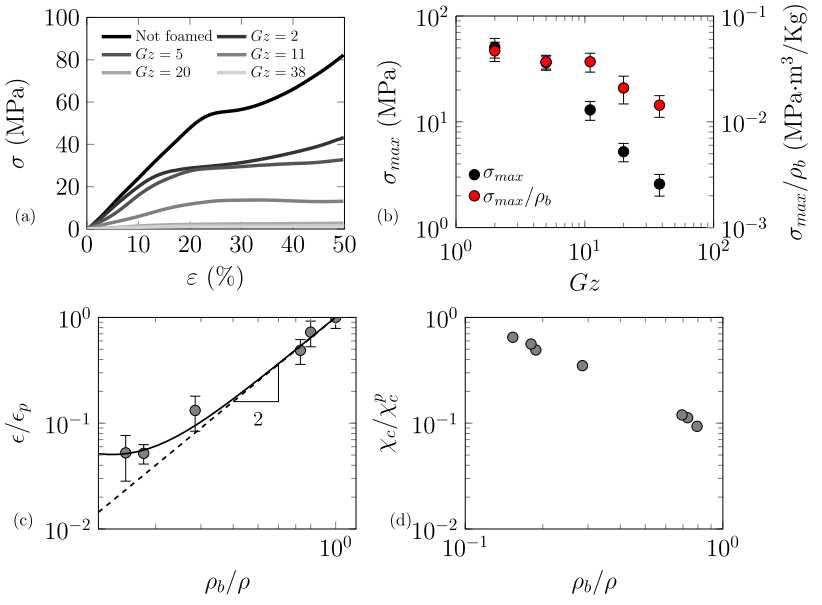

Figure 11. (a) Stress (σ)-strain (ε) curves of foamed and nonfoamed PET strands under compression, with different levels of foaming characterized by *Gz*. (b) Maximum stress (σ_{max}) and specific maximum stress (σ_{max}/ρ_b) as functions of the Graetz number. (c) Specific elastic modulus (ϵ/ϵ_p) as a function of the inverse expansion ratio (ρ_b/ρ). The data follows a power-law with slope −2 (dashed line) at higher densities. The solid line represents the scaling provided in eq 4. (d) Specific crystallinity (χ_c/χ_c^p) as a function of the inverse expansion ratio.

https://doi.org/10.1021/acs.iecr.5c01123
Ind. Eng. Chem. Res. 2025, 64, 12770−12780

governs the extent of crystal melting. For $Gz < 10$, a nearly uniform temperature distribution leads to full melting of the crystals, resulting in low crystallinity and poor foam expansion. In contrast, when $Gz > 10$, significant thermal gradients promote the preservation of some crystals, which act as heterogeneous nucleation sites and improve foam quality in terms of expansion ratio, cell density, and uniformity.

Mechanical testing confirmed that increased foaming reduces absolute compressive strength, as expected due to increased porosity. However, the specific mechanical properties (normalized by density) remain relatively stable across a wide range of conditions, indicating good mechanical efficiency. To describe this behavior, a modified scaling law was proposed, which accounts for the reinforcing effect of crystallinity on the elastic modulus of the foamed strands.

The elimination of chemical additives such as chain extenders offers both economic and sustainability advantages. Not only are processing costs reduced, but the absence of molecular branching promotes higher crystallinity, which in turn enhances both mechanical and rheological performance. This makes the proposed method a viable route for fabricating lightweight, high-performance polymer structures in industrial applications.

To further advance this approach, future research should examine the effects of additional process parameters such as CO_2 saturation pressure, duration, and hot-end temperature, which are expected to further influence crystallinity and foam structure. It would also be valuable to conduct control experiments using precrystallized PET filaments without CO_2 saturation, in order to isolate the role of thermal gradients in crystal melting. Although technically challenging—since crystallinity in PET is closely linked to CO_2 solubilization—such studies would help confirm whether the observed behavior is due solely to thermal effects or to interactions between saturation and foaming. In addition, while the present study focused on individual foamed strands, a critical next step is to fabricate multistrand or layered printed structures. This will enable mechanical testing of interstrand adhesion and interfacial strength, which is essential to assess the feasibility of scaling the process for structural applications. Literature suggests that when thermoplastic strands are deposited in a molten state, they can form strong cohesive interfaces via polymer chain entanglement, potentially allowing the creation of robust, load-bearing 3D foam architectures.

In conclusion, this study provides a promising pathway toward scalable, sustainable, and cost-effective production of structured polymer foams via additive manufacturing, opening new opportunities for high-performance lightweight materials without the need for chemical modification. Moreover, the underlying principle—leveraging gas-induced crystallinity and thermal gradient control to direct foam structure—could be extended beyond engineering polymers. In particular, this approach holds potential for applications in food systems,[42] where additive-free foaming, controlled porosity, and tailored mechanical properties are equally desirable for developing novel textures and functional food structures through 3D printing.

■ ASSOCIATED CONTENT

Supporting Information

The Supporting Information is available free of charge at https://pubs.acs.org/doi/10.1021/acs.iecr.5c01123.

Heat transfer modeling and simulation; nozzle geometry used in the simulations (Figure S1); temperature distribution within the 3D printing nozzle for two different Graetz numbers (Figure S2); small amplitude oscillatory sweep of PET; storage and loss modulus of PET (Figure S3) (PDF)

■ AUTHOR INFORMATION

Corresponding Author

Lorenzo Lombardi − *Department of Chemical, Materials and Production Engineering, University of Naples Federico II, Naples 80125, Italy;* orcid.org/0000-0003-0511-347X; Email: lorenzo.lombardi@unina.it

Authors

Claudio Esposito − *Department of Chemical, Materials and Production Engineering, University of Naples Federico II, Naples 80125, Italy;* orcid.org/0000-0003-4956-6227

Daniele Tammaro − *Department of Chemical, Materials and Production Engineering, University of Naples Federico II, Naples 80125, Italy;* orcid.org/0000-0001-7340-0951

Odda Ruiz de Ballesteros − *Department of Chemical Sciences, University of Naples Federico II, Complesso Monte Sant'Angelo, Naples 80126, Italy*

Pier Luca Maffettone − *Department of Chemical, Materials and Production Engineering, University of Naples Federico II, Naples 80125, Italy*

Complete contact information is available at: https://pubs.acs.org/10.1021/acs.iecr.5c01123

Notes

The authors declare no competing financial interest.

■ REFERENCES

(1) Suhaimi, N. A. S.; Muhamad, F.; Abd Razak, N. A.; Zeimaran, E. Recycling of polyethylene terephthalate wastes: A review of technologies, routes, and applications. *Polym. Eng. Sci.* **2022**, *62*, 2355−2375.

(2) Nisticò, R. Polyethylene terephthalate (PET) in the packaging industry. *Polym. Test.* **2020**, *90*, No. 106707.

(3) Sojobi, A. O.; Nwobodo, S. E.; Aladegboye, N. Recycling of polyethylene terephthalate (PET) plastic bottle wastes in bituminous asphaltic concrete. *Cogent Eng.* **2016**, *3*, No. 1133480, DOI: 10.1080/23311916.2015.1133480.

(4) Kamrani, H.; Nosrati, A. Fabrication of Nanofiber Filtration Membranes Using Polyethylene Terephthalate (PET): A Review. *J. Membr. Sci. Technol.* **2018**, *08*, No. 1000183, DOI: 10.4172/2155-9589.1000183.

(5) Jafari, S.; Hosseini Salekdeh, S. S.; Solouk, A.; Yousefzadeh, M. Electrospun polyethylene terephthalate (PET) nanofibrous conduit for biomedical application. *Polym. Adv. Technol.* **2020**, *31*, 284−296.

(6) Sulyman, M.; Haponiuk, J.; Formela, K. Utilization of Recycled Polyethylene Terephthalate (PET) in Engineering Materials: A Review. *Int. J. Environ. Sci. Dev.* **2016**, *7*, 100−108.

(7) Liu, H.; Antwi-Afari, M. F.; Mi, H.; Liu, C. Research on the feasibility of polyethylene terephthalate foam used in wind turbine blades. *Environ. Prog. Sustainable Energy* **2023**, *42*, No. e13956.

(8) Donahue, C. J.; Exline, J. A.; Warner, C. Chemical recycling of pop bottles: The synthesis of dibenzyl terephthalate from the plastic polyethylene terephthalate. *J. Chem. Educ.* **2003**, *80*, 79−82.

(9) Xanthos, M.; Yilmazer, U.; Dey, S. K.; Quintans, J. Melt viscoelasticity of polyethylene terephthalate resins for low density extrusion foaming. *Polym. Eng. Sci.* **2000**, *40*, 554−566.

(10) Xanthos, M.; Wan, C.; Dhavalikar, R.; Karayannidis, G. P.; Bikiaris, D. N. Identification of rheological and structural characteristics of foamable poly(ethylene terephthalate) by reactive extrusion. *Polym. Int.* **2004**, *53*, 1161−1168.

(11) Tammaro, D.; Lombardi, L.; Maffettone, P. L. Bimodal cell distributions in foaming of olefin block copolymers using high-throughput experimentation. *Chem. Eng. Sci.* **2025**, *304*, No. 121067.
(12) Yao, S.; Guo, T.; Liu, T.; Xi, Z.; Xu, Z.; Zhao, L. Good extrusion foaming performance of long-chain branched PET induced by its enhanced crystallization property. *J. Appl. Polym. Sci.* **2020**, *137*, No. 49268, DOI: 10.1002/app.49268.
(13) Li, D.; Liu, T.; Zhao, L.; Yuan, W. Controlling sandwich-structure of PET microcellular foams using coupling of CO2 diffusion and induced crystallization. *AIChE J.* **2012**, *58*, 2512−2523.
(14) Baldwin, D. F.; Park, C. B.; Suh, N. P. A microcellular processing study of poly(ethylene terephthalate) in the amorphous and semicrystalline states. Part II: Cell growth and process design. *Polym. Eng. Sci.* **1996**, *36*, 1446−1453.
(15) Baldwin, D. F.; Park, C. B.; Suh, N. P. A microcellular processing study of polyethylene terephthalate in the amorphous and semicrystalline states. Part I: Microcell nucleation. *Polym. Eng. Sci.* **1996**, *36*, 1437−1445.
(16) Lambert, S. M.; Paulaitis, M. E. Crystallization of poly(ethylene terephthalate) induced by carbon dioxide sorption at elevated pressures. *J. Supercrit. Fluids* **1991**, *4*, 15−23.
(17) Mizoguchi, K.; Hirose, T.; Naito, Y.; Kamiya, Y. CO2-induced crystallization of poly(ethylene terephthalate). *Polymer* **1987**, *28*, 1298−1302.
(18) Kwon, D. E.; Aregay, M. G.; Park, B. K.; Lee, Y. W. Preparation of polyethylene terephthalate foams at different saturation temperatures using dual methods of supercritical batch foaming. *Korean J. Chem. Eng.* **2021**, *38*, 2560−2566.
(19) Tammaro, D.; Chacon, F. A.; Schennink, G.; Walker, C.; Trommsdorff, U. Extrusion Foam of Polylactic Acid Using Stereocomplex Crystals. *Polym. Foams* **2022**, 253−273.
(20) Kruse, M.; Wagner, M. H. Rheological and molecular characterization of long-chain branched poly(ethylene terephthalate). *Rheol. Acta* **2017**, *56*, 887−904.
(21) Härth, M.; Kaschta, J.; Schubert, D. W. Shear and elongational flow properties of long-chain branched poly(ethylene terephthalates) and correlations to their molecular structure. *Macromolecules* **2014**, *47*, 4471−4478.
(22) Dolatshah, S.; Ahmadi, S.; Ershad Langroodi, A.; Alavi, A. Long-chain branching of polyethylene terephthalate: Rheological/thermal properties of polyethylene terephthalate/carbon nanotube nanocomposite. *Polym. Eng. Sci.* **2022**, *62*, 2322−2334.
(23) Coccorullo, I.; Di Maio, L.; Montesano, S.; Incarnato, L. Theoretical and experimental study of foaming process with chain extended recycled PET. *eXPRESS Polym. Lett.* **2009**, *3*, 84−96.
(24) Sova, N.; Savchenko, B.; Beloshenko, V.; Slieptsov, A.; Vozniak, I. Sorption Properties of PET Copolyesters and New Approach for Foaming with Filament Extrusion Additive Manufacturing. *Polymers* **2023**, *15*, No. 1138.
(25) Sorrentino, L.; Di Maio, E.; Iannace, S. Poly(ethylene terephthalate) foams: Correlation between the polymer properties and the foaming process. *J. Appl. Polym. Sci.* **2010**, *116*, 27−35.
(26) Xia, T.; Xi, Z.; Liu, T.; Pan, X.; Fan, C.; Zhao, L. Melt foamability of reactive extrusion-modified poly(ethylene terephthalate) with pyromellitic dianhydride using supercritical carbon dioxide as blowing agent. *Polym. Eng. Sci.* **2015**, *55*, 1528−1535.
(27) Bocz, K.; Ronkay, F.; Molnár, B.; Vadas, D.; Gyürkés, M.; Gere, D.; Marosi, G.; Czigany, T. Recycled PET foaming: Supercritical carbon dioxide assisted extrusion with real-time quality monitoring. *Adv. Ind. Eng. Polym. Res.* **2021**, *4*, 178−186.
(28) Tammaro, D.; Della Gatta, R.; Villone, M. M.; Maffettone, P. L. Continuous 3D Printing of Hierarchically Structured Microfoamed Objects. *Adv. Eng. Mater.* **2022**, *24*, No. 2101226, DOI: 10.1002/adem.202101226.
(29) Trofa, M.; Di Maio, E.; Maffettone, P. L. Multi-graded foams upon time-dependent exposition to blowing agent. *Chem. Eng. J.* **2019**, *362*, 812−817.
(30) Brandrup, J.; Immergut, E. H.; Grulke, E. A.; Abe, A.; Bloch, D. R.; Wlley, J.; Chichester, N. Y.; Brisbane, W.; Toronto, S. *Polymer Handbook* 1999.
(31) Tammaro, D. Rheological characterization of complex fluids through a table-top 3D printer. *Rheol. Acta* **2022**, *61*, 761−772.
(32) Cusano, I.; Campagnolo, L.; Aurilia, M.; Costanzo, S.; Grizzuti, N. Rheology of Recycled PET. *Materials* **2023**, *16*, No. 3358.
(33) Fan, C.; Wan, C.; Gao, F.; Huang, C.; Xi, Z.; Xu, Z.; Zhao, L.; Liu, T. Extrusion foaming of poly(ethylene terephthalate) with carbon dioxide based on rheology analysis. 2015; Vol. *52*, pp 277−298 DOI: 10.1177/0021955X14566085.
(34) Tammaro, D.; Astarita, A.; Di Maio, E.; Iannace, S. Polystyrene Foaming at High Pressure Drop Rates. *Ind. Eng. Chem. Res.* **2016**, *55*, 5696−5701.
(35) Yao, S.; Hu, D.; Xi, Z.; Liu, T.; Xu, Z.; Zhao, L. Effect of crystallization on tensile mechanical properties of PET foam: Experiment and model prediction. *Polym. Test.* **2020**, *90*, No. 106649.
(36) Chen, Y.; Yao, S.; Ling, Y.; Zhong, W.; Hu, D.; Zhao, L. Microcellular PETs with High Expansion Ratio Produced by Supercritical CO2 Molding Compression Foaming Process and Their Mechanical Properties. *Adv. Eng. Mater.* **2022**, *24*, No. 2101124, DOI: 10.1002/adem.202101124.
(37) Tammaro, D.; Villone, M. M.; Maffettone, P. L. Microfoamed Strands by 3D Foam Printing. *Polymers* **2022**, *14*, No. 3214.
(38) Esposito, C.; Tammaro, D.; Posabella, P.; Villone, M. M.; D'Avino, G.; Maffettone, P. L. Orientation-Graded Morphologies in Microcellular Foams through Additive Manufacturing. *Ind. Eng. Chem. Res.* **2024**, *63*, 17949−17960.
(39) Lombardi, L.; Roig-Sanchez, S.; Bapat, A.; Frostad, J. M. Nonaqueous foam stabilization mechanisms in the presence of volatile solvents. *J. Colloid Interface Sci.* **2023**, *648*, 46−55.
(40) Lakes, R. Materials with structural hierarchy. *Nature* **1993**, *361*, 511−515.
(41) Tammaro, D.; Ballesteros, A.; Walker, C.; Reichelt, N.; Trommsdorff, U. Expanded Beads of High Melt Strength Polypropylene Moldable at Low Steam Pressure by Foam Extrusion. *Polymers* **2022**, *14*, No. 205.
(42) Lombardi, L.; Consalvo, S.; Esposito, C.; Tammaro, D. Tailoring texture and functionality of vegetable protein meat analogues through 3D printed porous structures. *Food Hydrocolloids* **2025**, *159*, No. 110611.

https://doi.org/10.1021/acs.iecr.5c01123
Ind. Eng. Chem. Res. 2025, 64, 12770−12780